Top–down control on eruptive style at Masaya volcano inferred from melt composition

Lisa Hlinka [a,b,∗], Marc-Antoine Longpré [a,b], Wendy Pérez [c], Steffen Kutterolf [c], Brian Monteleone [d]

[a] School of Earth and Environmental Sciences, Queens College, City University of New York, Queens, NY 11367, USA
[b] Earth and Environmental Sciences, The Graduate Center, City University of New York, New York, NY 10016, USA
[c] GEOMAR, Helmholtz Centre for Ocean Research, Kiel, Germany
[d] Department of Geology and Geophysics, Woods Hole Oceanographic Institution, Woods Hole, MA 02543, USA

ARTICLE INFO

ABSTRACT

Highly explosive Plinian eruptions of basaltic magma are enigmatic because low melt viscosities should inhibit such eruptive style. Masaya volcano, Nicaragua, is a persistently active basaltic system capable of a wide range of eruptive styles, from open-conduit lava lake activity to voluminous Plinian eruptions; it is thus an ideal natural laboratory to constrain potential controls on basaltic eruption style. Here we report the major, trace, and volatile (CO_2, H_2O, S, Cl, F) element composition of olivine-, plagioclase- and clinopyroxene-hosted melt inclusions as well as matrix glasses from lava lake ejecta and two Plinian tephra deposits—the 2.1 ka Masaya Triple Layer and the 1.8 ka Ticuantepe Lapilli—to test whether pre-eruptive volatile contents and degassing history may be linked to eruptive style. All samples display a relatively narrow and largely overlapping basaltic–basaltic andesitic compositional range (51.7 ± 1.0 wt.% SiO_2, 4.8 ± 0.4 wt.% MgO) with similar trace element signatures (e.g., Ce/Y $= 0.82 \pm 0.10$, Ba/La $= 74 \pm 11$). However, lava lake and Plinian samples show systematic differences in pre-eruptive volatile contents, forming distinct groups with mean H_2O contents of 0.6 ± 0.2 wt.% (lava lake), 1.1 ± 0.2 wt.% (Masaya Triple Layer), and 1.9 ± 0.3 wt.% (Ticuantepe Lapilli). Together, these groups generate broad positive correlations between S, Cl and H_2O concentrations, with maximum values reaching 920 ppm, 1300 ppm and 2.3 wt.%, respectively, which are low compared to typical Central American arc magmas. Magma temperature estimates overlap and average at $1115 \pm 30\,°C$, while volatile saturation pressures are low, mainly <100 MPa, although only lava lake samples record pressures <31 MPa. These observations reiterate the compositionally buffered state of the volcano's magmatic system highlighted by previous work and demonstrate that — regardless of eruption style — all Masaya magmas undergo variable, but extensive, pre-eruptive degassing at low pressure. Geohygrometry, gas emissions, and H_2O/Ce–Ba/La systematics suggest initial, undegassed H_2O contents on the order of 3.9–5.5 wt.%. Our results imply that pre-eruptive volatile contents are not the culprit for Plinian events at Masaya. Instead, we propose that the volcano's vigorous magma supply is modulated in a top–down manner to produce a wide range of eruptive styles, whereby temporary sealing of the conduit may instigate a transition to explosive behavior. In this model, rapid magma ascent is triggered when the seal eventually breaks from degassing-induced pressurization, yielding high degrees of undercooling, rapid microlite growth, and a dramatic increase in magma viscosity and explosive eruption potential. There may thus be a thin line between open-conduit conditions and Plinian eruptions at Masaya.

© 2021 Elsevier B.V. All rights reserved.

1. Introduction

Explosive volcanic eruptions of Plinian style are usually associated with magmas characterized by intermediate to high silica content and high viscosity. Basaltic magmas, on the other hand, have low melt viscosities that generally inhibit magma fragmentation and promote effusive or mildly explosive eruptive styles (e.g., Cassidy et al., 2018). The occurrence, albeit rare, of basaltic tephra

∗ Corresponding author at: Earth and Environmental Sciences, The Graduate Center, City University of New York, New York, NY 10016, USA.
E-mail address: lhlinka@gradcenter.cuny.edu (L. Hlinka).

deposits of Plinian character (e.g., Williams, 1983) is thus puzzling and has fueled energetic research in the past two decades (e.g., Arzilli et al., 2019; Goepfert and Gardner, 2010; Houghton and Gonnermann, 2008; Moitra et al., 2018). Factors other than melt viscosity have been proposed to promote explosive behavior at basaltic volcanoes, including (1) initially high volatile content (particularly H_2O and CO_2) increasing magma buoyancy and overpressure during ascent (e.g., Helo et al., 2011; Roggensack et al., 1997; Sides et al., 2014); (2) fragmentation of bubbly magma due to brittle failure of bubbles (e.g., Zhang, 1999); (3) high magma ascent rate preventing efficient gas–melt segregation (e.g., Barth et al., 2019; Goepfert and Gardner, 2010); and (4) syn-eruptive microlite growth yielding an increase in magma viscosity (e.g., Arzilli et al., 2019; Houghton and Gonnermann, 2008; Moitra et al., 2018). However, these factors may be interrelated — e.g., high pre-eruptive volatile contents may favor fast magma ascent — and it remains difficult to isolate a dominating mechanism for explosive basaltic volcanism (Cassidy et al., 2018).

Masaya volcano, Nicaragua, is a basaltic arc volcano that shows little variation in magma composition over time but a dramatic range of eruptive styles, from open-conduit lava lake activity to voluminous Plinian fall deposits (Pérez et al., 2009, 2020; Walker et al., 1993; Williams, 1983; Zurek et al., 2019). Thus, it represents an ideal natural laboratory to test ideas on eruptive style controls at basaltic volcanoes. The volcano comprises two main cones and three pit craters within a large and elongated (6×11 km) caldera (Fig. S1). It is associated with the older Las Sierras Formation, forming a prominent topographic high, and complex tectonics, including extensional structures (Funk et al., 2009; Girard and van Wyk de Vries, 2005). In historical times, Masaya has been persistently active and characterized by open-conduit conditions, producing prodigious gas emissions, common lava lakes (which most recently reemerged in December 2015 (Aiuppa et al., 2018)), but little to no erupted material (Martin et al., 2010; Walker et al., 1993). Yet, volatile budgets indicate that magma supply is high, with a recent estimate at $\sim$0.19 km^3 per year, suggesting that up to 47 km^3 of magma may have degassed since the last effusive eruption in 1772, almost 250 years ago (Zurek et al., 2019). The large discrepancy between degassed and erupted magma volumes at Masaya and other persistently active basaltic systems can be explained by convection of magma within a shallow conduit linked to a deeper reservoir as well as by endogenous volcano growth (e.g., de Moor et al., 2013; Francis et al., 1993; Shinohara, 2008; Stix, 2007). Drastically contrasting with its historical behavior, Masaya has also generated three highly explosive basaltic eruptions in the Holocene, each producing widespread pyroclastic deposits 2–9 km^3 (dense rock equivalent−DRE) in volume−the $\sim$6 ka San Antonio Tephra, the $\sim$2.1 ka Masaya Triple Layer, and the $\sim$1.8 ka Masaya Tuff with associated Ticuantepe Lapilli (Kutterolf et al., 2008; Pérez and Freundt, 2006; Pérez et al., 2009, 2020). Older deposits of explosive basaltic volcanism associated with Masaya and Las Sierras also exist (e.g., Costantini et al., 2010; Girard and van Wyk de Vries, 2005). Previous work attributed Masaya's enigmatic Plinian events to rapid ascent ($\sim$1 ms^{-1}) of magma from great depths ($\sim$100 km) (Gregg and Williams, 1996) or, more recently, to rapid syn-eruptive microlite crystallization (Arzilli et al., 2019; Bamber et al., 2020).

In this paper, we utilize melt inclusions, which are parcels of melt trapped during crystal growth (e.g., Métrich and Wallace, 2008), to test whether pre-eruptive volatile contents and degassing history may be linked to eruptive style at Masaya. New major, trace, and volatile (CO_2, H_2O, S, Cl, F) element data are presented for olivine-, plagioclase- and clinopyroxene-hosted melt inclusions and their host matrix glasses sampled from lava lake (LL) ejecta and two Plinian deposits−the Masaya Triple Layer (MTL) and the Ticuantepe Lapilli (TIL). Results are discussed in the context of pre-

vious work and point to differences in shallow decompression history of magma controlling eruptive style. A model is proposed in which eruptive style is modulated in a top–down fashion; temporary sealing of the system paired with vigorous gas accumulation may generate a cascade effect sufficient to transition to explosive behavior.

2. Methodology

2.1. Samples

Lava lake ejecta samples, representing open-conduit conditions and consisting of wind-blown Pele's hairs and scoria lapilli, were collected in 2016, 2017, and 2018 along the rim of the active Santiago crater. As representative products of Masaya's Plinian eruptions, we selected samples of the MTL and TIL lapilli fall deposits collected by Pérez and Freundt (2006) that bear sufficient amounts of phenocrysts larger than 250 μm. In the field, the MTL fall deposits, with an estimated volume of 2 km^3 DRE (Pérez et al., 2020), include seven major beds of well-sorted scoriaceous lapilli to coarse ash, divided by several major and minor tuff layers (Pérez et al., 2009). MTL lapilli contain <5 vol% of olivine, plagioclase, and clinopyroxene phenocrysts in a vesicular sideromelane groundmass (Pérez and Freundt, 2006). The TIL fall deposits directly overlie the associated Masaya Tuff (MT) and include four well-sorted scoria lapilli layers, divided by three ash-rich layers. The combined volume of MT and TIL is estimated at 2 km^3 DRE (Pérez et al., 2020). TIL lapilli contain $\sim$5% phenocrysts in a vesicular microlite-rich tachylitic groundmass (Pérez and Freundt, 2006). Plagioclase is the most abundant phenocryst phase, followed by olivine, then clinopyroxene. Sample localities and corresponding eruptive units used in this study are given in Fig. S1.

Phenocrysts of olivine, plagioclase, and clinopyroxene were handpicked or extracted through heavy liquid separation from crushed and sieved lapilli for each eruption. After cleaning in a sonic bath, the phenocrysts were mounted in epoxy and polished to expose the melt inclusions, then transferred to an indium mount prior to analysis. We targeted glassy, rounded to elliptical melt inclusions generally 25–150 μm in diameter, lacking evidence of leakage (Fig. 1). When possible, we favored bubble-free inclusions to avoid the possible effect of volatile (e.g., CO_2, S) loss to vapor bubbles (e.g., Moore et al., 2015; Rasmussen et al., 2020; Venugopal et al., 2020). While all LL and 36% of MTL inclusions selected are bubble-free, all TIL and 64% of MTL inclusions contain at least one vapor bubble. Most bubble-bearing melt inclusions contain a single bubble <1–20 μm in diameter, with bubble size appearing to scale up with melt inclusion size. Further sample description details are provided in the Supplementary Materials and Fig. S2.

2.2. Secondary ion mass spectrometry (SIMS)

SIMS analyses were conducted on a Cameca IMS 1280 instrument at Woods Hole Oceanographic Institution to measure volatile (CO_2, H_2O, S, F and Cl) concentrations in a total of 48 melt inclusions (23 from LL, 14 from MTL, and 11 from TIL) and 18 matrix glass or Pele's hair chips (12 from LL, 3 from MTL, and 3 from TIL). Sample preparation protocols and analytical procedures are based on Hauri et al. (2002); see also Longpré et al. (2017) and the Supplementary Materials for details. Calibration curves for $^{12}C/^{30}Si$, $^{16}O^1H/^{30}Si$, $^{19}F/^{30}Si$, $^{32}S/^{30}Si$ and $^{35}Cl/^{30}Si$ versus the respective volatile component were established using eight basaltic to basaltic andesite glass standards (Fig. S3). The standard error on the slope of the calibration curves is 1.8% or better for all volatiles. Repeated analysis ($n = 8$) of standard ALV519-4-1, a MORB glass, throughout our analytical session yielded 162 ± 4 ppm CO_2, 0.15 ± 0.01 wt.% H_2O, 105 ± 2 ppm F, 862 ± 14 ppm S, and 43 ± 1 ppm Cl
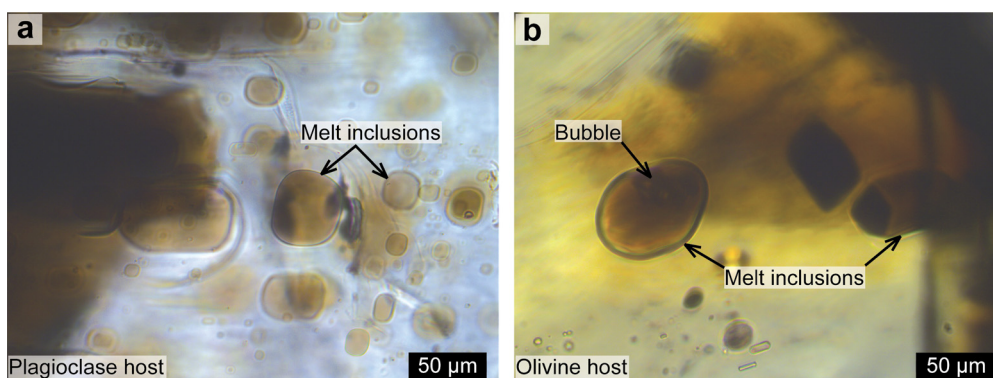
Fig. 1. Photomicrographs of Masaya samples showing representative melt inclusions. (a) Bubble-free plagioclase-hosted melt inclusions from a lava lake sample. (b) Bubble-bearing olivine-hosted melt inclusions from a MTL Plinian sample.

(Fig. S4); this agrees well with published values provided in Table S1. Spot analyses of host mineral adjacent to melt inclusions yielded <3 ppm CO_2, <0.003 wt.% H_2O, <1 ppm F, <1 ppm S, and <1 ppm Cl, demonstrating low analytical backgrounds. Additional information on SIMS data quality is presented in the Supplementary Materials.

2.3. Electron probe micro-analysis (EPMA)

After SIMS work, major element compositions of melt inclusions and matrix glasses were obtained using a Cameca SX-100 electron microprobe at the American Museum of Natural History. Analyses were conducted using an acceleration voltage of 15 kV, a beam current of 10 nA, and beam diameters of 5 μm, 10 μm, or 15 μm, depending on the size of available glass patches. Repeated analyses of our in-house standard P1326-2, a Juan de Fuca Ridge basaltic glass, demonstrate accuracy better than 2.4% relative for major elements over 1 wt.% concentration (Table S2). Analyses of melt inclusion host minerals were also performed, but restricted to a few points per crystal, at its core and rim as well as adjacent to the melt inclusion. In addition, after point analysis, we acquired X-ray intensity maps of 12 melt inclusions selected to reflect the full compositional range of our samples. Further details on the setup of X-ray maps and EPMA data quality are provided in the Supplementary Materials.

2.4. Laser ablation inductively coupled plasma mass spectrometry (LA-ICP-MS)

As a final analytical step, trace element concentrations in melt inclusions and matrix glasses were acquired by LA-ICP-MS at the Lamont-Doherty Earth Observatory of Columbia University, with a New Wave UP193-FX laser ablation system paired with a Thermo VG PQ ExCell mass spectrometer. Analytical conditions comprised a 8-Hz repetition rate and a fluency of ∼9.8 J/cm^2 on the sample surface. Calibration curves were established using repeated in-run analysis of basaltic glass standards, BIR-1, BHVO-2, and BCR-2 (Table S3). Melt inclusions were analyzed at various spot sizes (40, 25 and 10 μm) depending on the diameter of the inclusion, and matrix glasses were analyzed with 50 or 75 μm diameter spots. Repeated in-run analyses of two secondary glass standards, P1326-2 and ALV519-4-1, indicate that our measurements lie within 4% standard error for most trace elements (Table S3).

2.5. Assessment of post-entrapment modification of melt inclusions

Potential post-entrapment modification of our melt inclusions was assessed via a three-fold approach: (1) compositions of melt inclusion were compared to matrix glass and published bulk rock values to flag any anomalous composition with respect to Masaya's liquid line of descent (Fig. S5); (2) elemental X-ray maps of 12 representative melt inclusions were screened for homogeneity within each melt inclusion and across the melt inclusion–host mineral interface (Fig. 2); and (3) for olivine-hosted melt inclusions showing evidence of post-entrapment modification in (1) and/or (2), we performed a correction using Petrolog3 (Fig. S6; Danyushevsky and Plechov, 2011), assuming an oxygen fugacity of 1.7 log units above the fayalite–magnetite–quartz (FMQ) buffer (de Moor et al., 2013), host Fo% content adjacent to melt inclusions, and initial melt FeO_t estimated from a SiO_2–FeO_t linear regression of the liquid line of descent. Most olivine-hosted inclusions required <5% correction. However, two small inclusions from the TIL samples show evidence of extensive post-entrapment modification requiring up to 23% correction; these inclusions are excluded from further discussion but are reported in Table S4. Plagioclase-hosted melt inclusions show little to no evidence of significant post-entrapment modification and thus were not corrected (Figs. 2, S7). Further details on correction methods and equilibrium K_D values are described in the Supplements. For olivine-hosted melt inclusions, the text and figures present corrected data only, while both raw and corrected data are listed in full in Supplementary Tables S4–S5.

3. Results

3.1. Major elements

Major element data reported in Fig. 3 reveal that our matrix glasses and melt inclusions hosted in olivine, plagioclase, and clinopyroxene phenocrysts display a relatively narrow basaltic–basaltic andesitic major element composition range, within e.g., 49.9–54.4 wt.% SiO_2, 3.8–5.8 wt.% MgO, and 0.9–1.7 wt.% K_2O. These results overlap with bulk rock and glass measurements from earlier studies at Masaya (Carr, 1984; Costantini et al., 2010; Goepfert and Gardner, 2010; Pérez, 2007; Sadofsky et al., 2008; Walker et al., 1993; Williams, 1983; Zurek et al., 2019). Strikingly, both in our dataset and published data, there is a general lack of significant correlation between major elements and MgO or SiO_2 contents, which limits their use as magma differentiation indices.

In detail, the compositions of melt inclusions from open-conduit LL and Plinian MTL samples generally overlap, except for two MTL plagioclase-hosted melt inclusions that show anomalously high FeO* coupled to low Al_2O_3, which may reflect minor post-entrapment crystallization (Fig. 3c,d). In comparison, the Plinian TIL melt inclusions display distinctly higher Al_2O_3 and appear slightly more primitive, though still fall within the range of published data (Fig. 3c). One TIL olivine-hosted melt inclusion shows anomalously high SiO_2 and low CaO (Fig. 3b,e). We do not
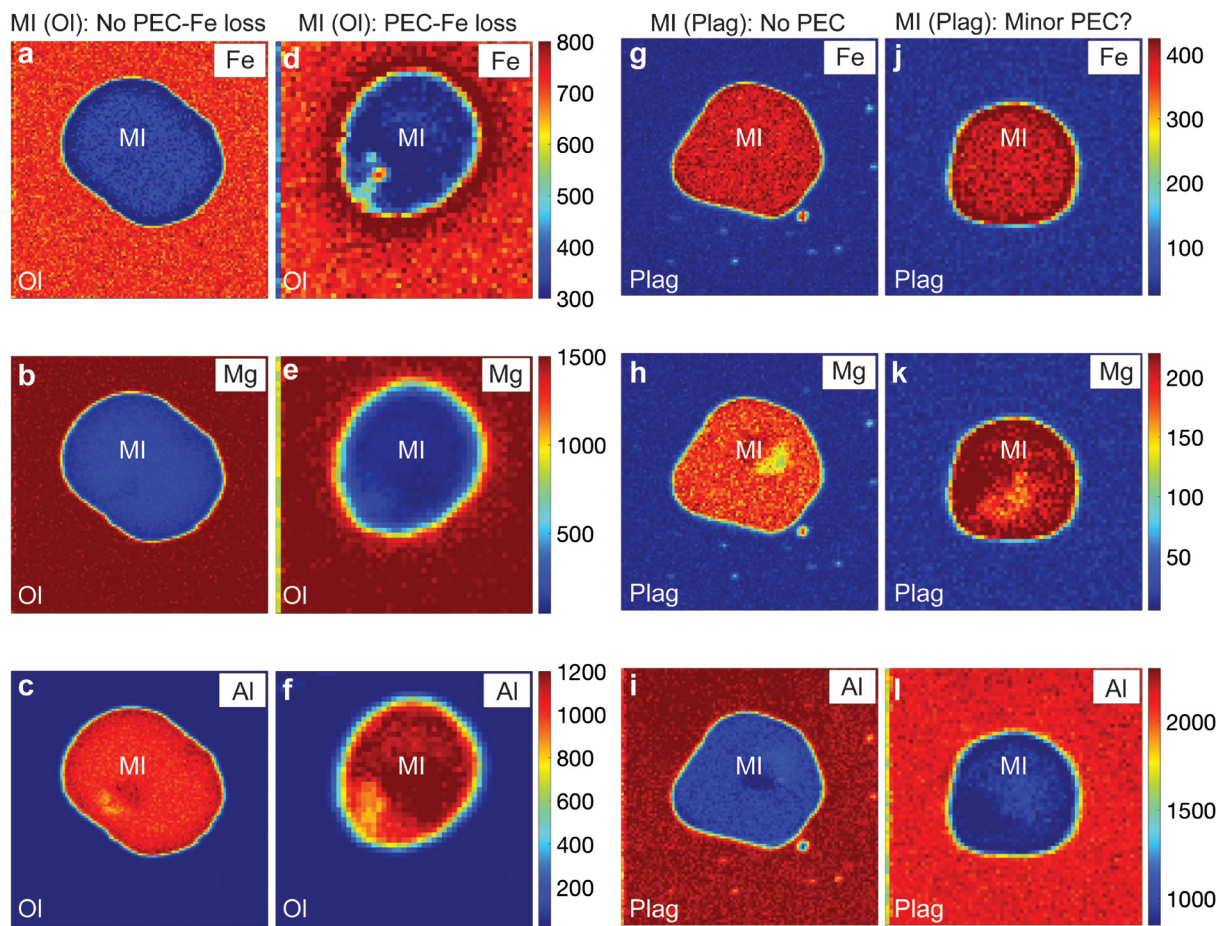
Fig. 2. Elemental maps of olivine- and plagioclase-hosted melt inclusions used to assess post-entrapment modification. Examples of olivine-hosted melt inclusions displaying no evidence (a–c) vs. clear evidence (d–f) for PEC and Fe-loss are shown. Maps of plagioclase-hosted melt inclusions indicate homogeneous compositions (g–i) to minor compositional modification (j–l). Color bars show signal intensity (blue: low; red: high). Maps are constructed with EPMA data (rastered using a 1 µm step size). From left to right, panel width is 110 µm (a–c), 51 µm (d–f), 101 µm (g–i), and 65 µm (j–l). A SIMS pit is present within each melt inclusion. (For interpretation of the colors in the figure(s), the reader is referred to the web version of this article.)

observe correlations between the major element compositions of melt inclusions and those of their host minerals.

Focusing on matrix glasses, the microlite-poor MTL glass chips and LL lapilli and Pele's hairs show restricted and nearly identical compositions that fall near the center of their respective melt inclusion data field. In comparison, the TIL glass exhibits greater compositional variability, records slightly lower MgO and CaO and higher SiO_2, Al_2O_3, and K_2O contents, and is significantly more evolved than TIL melt inclusions (Fig. 3); we attribute these features, at least in part, to the presence of abundant microlites in this tephra.

The observed compositional ranges of melt inclusion host minerals are Fo_{70-75} for olivine, An_{66-90} for plagioclase and $Mg\#_{72-75}$ for clinopyroxene. Though minor normal zoning is observed in a few olivines, plagioclase shows greater chemical zonation (Figs. S2, S7). By eruption, plagioclase from LL displays the widest and most evolved compositional range (An_{66-82}), followed by MTL (An_{78-89}), while TIL is characterized by the narrowest and most calcic composition (An_{86-90}).

3.2. Trace elements

In contrast to major elements displaying minor variability, several trace elements show relatively wide concentration ranges in our samples. High field strength zirconium, for example, varies by more than a factor of three, from 50 to 170 ppm, showing no correlation with MgO (Fig. 3g). Other incompatible trace elements,

such as Y, are positively correlated with Zr and span much of the range displayed by mafic–intermediate melt inclusions from across the Central American Volcanic Arc (Fig. 4a) (Sadofsky et al., 2008). However, the Ce/Y ratio, a proxy for the slope of the rare earth element pattern and thus the degree of enrichment, varies little (0.82 ± 0.10) and is not correlated with Zr concentration (Fig. 4b). Similarly, in terms of the Ba/La ratio, which is commonly used as a subduction component proxy, our samples yield a relatively narrow mean of 74 ± 11, at the upper mid-range for Central American melt inclusions and invariant with Zr (Fig. 4c). These observations indicate that the significant variation in trace element abundances in our samples is dominantly controlled by crystallization, with no evidence for changing source composition or degree of melting playing a role.

Zirconium and other incompatible trace elements are therefore much more sensitive indices of crystallization than major elements at Masaya. The Y–Zr relationship shown in Fig. 4a thus reflects melt inclusion entrapment occurring after variable extents of crystallization. Notably, the matrix glass and olivine-hosted melt inclusions from the LL and MTL have higher Y and Zr than those of TIL, consistent the slightly more primitive character of the latter as hinted by major elements.

Fig. 5 reports rare earth element data which show similar patterns for each eruption and fall within the upper range of previously published melt inclusion (Zurek et al., 2019) and bulk rock data for Masaya (e.g., Carr et al., 2014). Specifically, matrix glasses from LL and MTL yield nearly identical rare earth element concen-
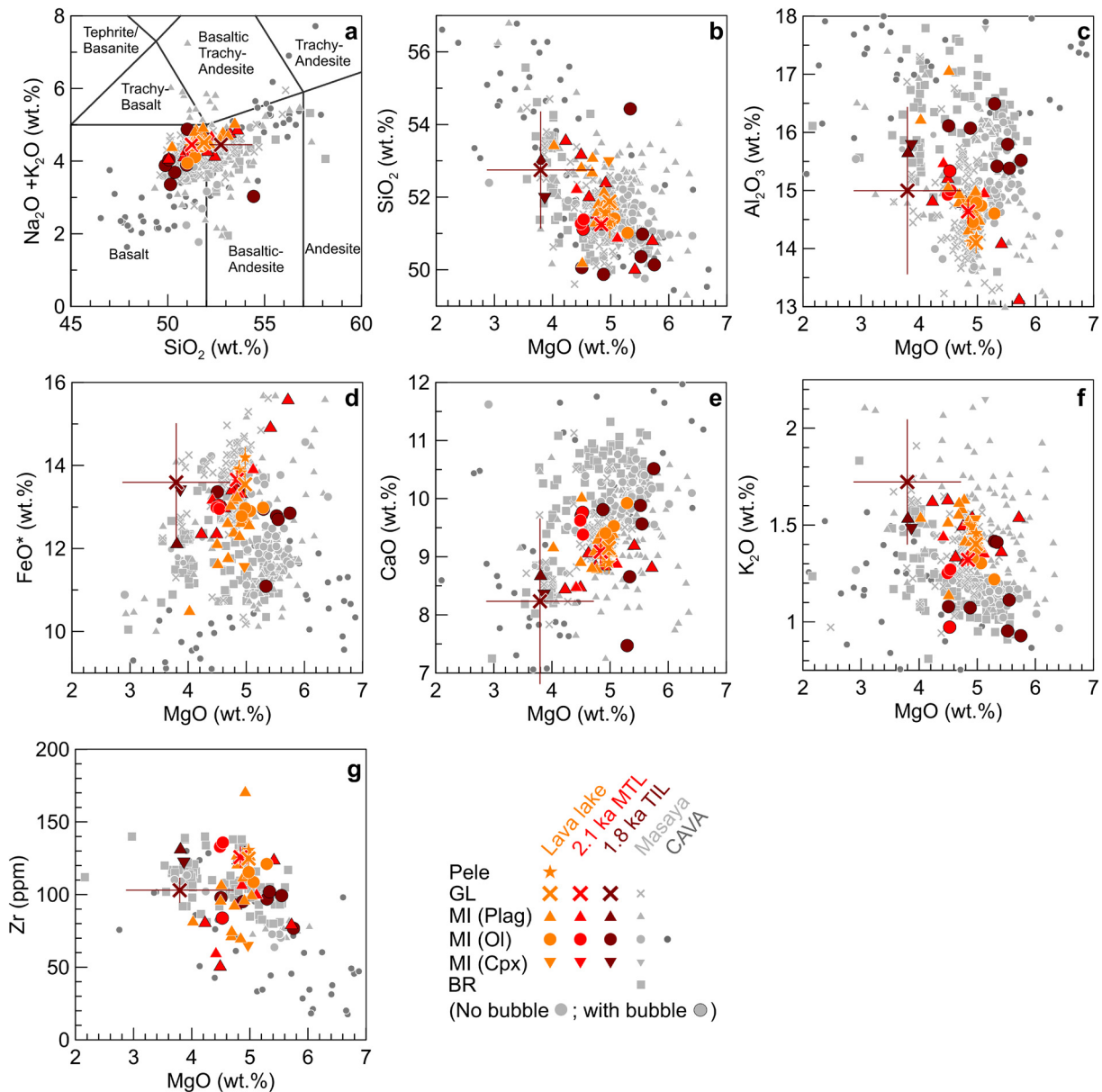
Fig. 3. Major element compositions for olivine-, plagioclase-, and clinopyroxene-hosted melt inclusions (MI (Ol), MI (Plag), and MI (Cpx)), matrix glasses (GL) and Pele's hairs (Pele) for our samples as compared to previously published bulk rock (BR), melt inclusion and matrix glass data from Masaya (Carr, 1984; Costantini et al., 2010; Goepfert and Gardner, 2010; Pérez, 2007; Sadofsky et al., 2008; Walker et al., 1993; Williams, 1983; Zurek et al., 2019) and melt inclusions from the Central American Volcanic Arc (CAVA; Sadofsky et al., 2008). (a) Total alkalis vs. SiO$_2$ diagram; (b) SiO$_2$, (c) Al$_2$O$_3$, (d) FeO*, (e) CaO, (f) K$_2$O, and (g) Zr vs. MgO. In these and all following plots, mean matrix glass and Pele's hair compositions are shown with 1σ error bars (not shown when smaller than symbol size). For melt inclusions, symbols with a white outline indicate bubble-free inclusions, whereas symbols with a black outline represent bubble-bearing inclusions.
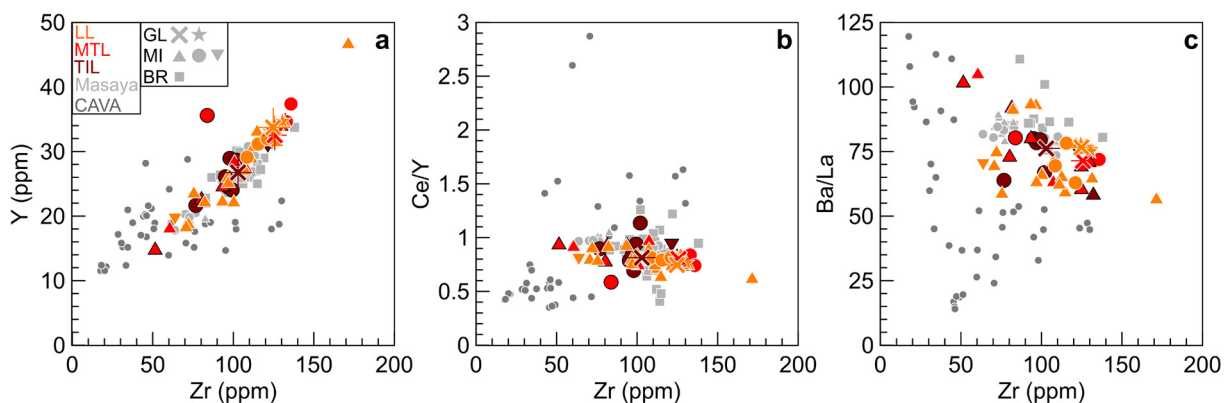

Fig. 4. Selected trace element variation diagrams. (a) Y, (b) Ce/Y, and (c) Ba/La vs. Zr. Symbols and published data sources as in Fig. 3.
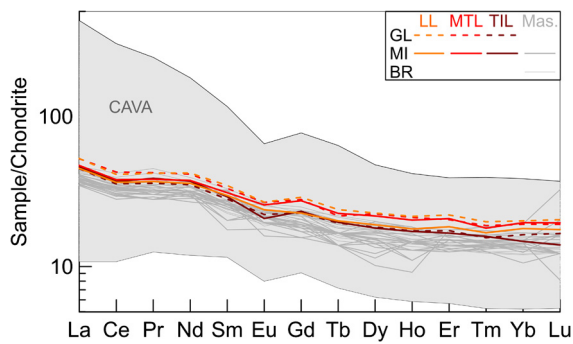
Fig. 5. Chondrite-normalized (McDonough and Sun, 1995) rare earth element diagram for average melt inclusion and matrix glass compositions compared with published data for Masaya and CAVA shown as shaded gray region (Zurek et al., 2019; Carr et al., 2014; and the GEOROC database (http://georoc.mpch-mainz.gwdg.de/georoc/; see Supplemental References). Our samples display subdued europium anomalies (Eu/Eu* = Eu$_N$/(Sm$_N$ × Gd$_N$)$^{0.5}$), with matrix glasses showing lower means and standard deviations (0.85 ± 0.04 for LL, 0.88 ± 0.08 for MTL, and 0.88 ± 0.02 for TIL) than melt inclusions (0.96 ± 0.32 for LL, 0.90 ± 0.16 for MTL, 0.87 ± 0.05 for TIL).

trations, while the TIL matrix glass records slightly lower values. Matrix glass and melt inclusions match well, particularly for MTL and TIL, consistent with a co-genetic link between the inclusions and carrier liquid. Moreover, we detect only very subtle negative europium anomalies in our samples, indicating limited plagioclase fractionation before and after melt inclusion entrapment.

3.3. Volatile elements

Marked differences between our samples begin to emerge in their volatile contents. Indeed, open-conduit LL and Plinian melt inclusions form distinct groups with mean H_2O contents of 0.6 ± 0.2 wt.% for LL, 1.1 ± 0.2 wt.% for MTL, and 1.9 ± 0.3 wt.% for TIL (Fig. 6). Within each group, there is little correlation between H_2O and other volatiles; however, the whole dataset displays broad positive correlations between S, Cl (and to a lesser extent F) and H_2O, e.g., mean melt inclusion sulfur concentrations increase from 130 ± 50 ppm for LL, 420 ± 240 ppm for MTL, to 680 ± 180 ppm for TIL (Fig. 6). In contrast, CO_2 concentrations show similar ranges across samples and, aside from five outliers, do not exceed 400 ppm. We also note that water content is not related to melt inclusion size, but — for plagioclase-hosted inclusions — it shows a broad positive correlation with the host anorthite content (Fig. S7).

As expected, the matrix glasses for each eruption are almost completely degassed in H_2O, CO_2, and S compared to melt inclusions (Fig. 6). An exception is observed for TIL glass patches which retain on average 144 ± 166 ppm CO_2 — the origin of this unexpected remnant CO_2 is unknown, but it may represent late-stage CO_2 supersaturation during magma ascent (e.g., Longpré et al., 2017). On the other hand, F and Cl concentrations remain significant in matrix glasses and generally sit at the low end of the melt inclusion range (Fig. 6c,d).

These results reveal significantly higher volatile contents in melt inclusions from Plinian fall deposits than from lava lake ejecta. However, even our highest measured concentrations are strikingly low with respect to typical maxima for mafic Central American arc magmas, which reach pre-eruptive H_2O, CO_2, S, Cl and F concentrations of ∼5.2 wt.%, 1800 ppm, 2540 ppm, 1930 ppm and 780 ppm, respectively (Fig. 6) (Sadofsky et al., 2008; Wehrmann et al., 2011). Our findings agree with previously published work at Masaya that reported modest maximum H_2O and S contents of 2.7 wt.% and 590 ppm, respectively (Bamber et al., 2020; Goepfert and Gardner, 2010; Pérez et al., 2020; Sadofsky et al., 2008; Zurek et al., 2019).

4. Discussion

In the following sections, we discuss our results in the context of previous work and outline arguments that: (1) reiterate the compositionally buffered state of Masaya's magmatic system; (2) constrain pre-eruptive conditions and demonstrate a key role for degassing at low pressure; (3) provide estimates of undegassed magmatic H_2O content; and (4) touch on the potential role of microlite crystallization in driving up magma viscosity. Integrating these lines of evidence, we then propose a model in which subtle changes in the uppermost plumbing system configuration control — in a top–down manner — the volcano's eruptive style.

4.1. A compositionally buffered system

Previous work has shown that the composition of Masaya's eruptive products varies little over the exposed stratigraphy, suggesting that its magmatic system has maintained a compositionally buffered, steady-state for at least 30,000–60,000 years (e.g., Kutterolf et al., 2008; Walker et al., 1993; Zurek et al., 2019). Minor compositional variations have been attributed to fractional crystallization of olivine, plagioclase and clinopyroxene in a large, shallow magma reservoir maintained by vigorous convection and periodic influx of less evolved basaltic magmas (Walker et al., 1993; Zurek et al., 2019). Our results are consistent with this view. As a striking example, the microlite-poor matrix glasses of LL and MTL, erupted ∼2100 years apart in dramatically contrasting fashion, are essentially indistinguishable chemically (Figs. 3–5). Particularly, we emphasize the restricted range of incompatible trace element ratios (e.g., Zr/Y, Ce/Y, Ba/La) in our samples which strongly suggests that primary magma compositions vary little. In other words, there is no evidence that magmas feeding the open-conduit and Plinian events are any different at the source. This is in stark contrast with the conclusions of Sides et al. (2014) at Kilauea volcano, where enriched melts (with e.g., high Ce/Y, high CO_2) may be predisposed to erupt more explosively. Such a bottom–up model, whereby primary magma composition would exert a first-order control on eruptive style variability, does not seem viable at Masaya.

4.2. Magmatic conditions and pre-eruptive degassing at low pressure

4.2.1. Temperature and pressure estimates

Our data, coupled to a series of geothermometers and geobarometers, allow estimation of pre-eruptive temperature and pressure conditions within Masaya's magmatic system. Fig. 7a shows a summary of temperature estimates obtained with olivine–melt (Putirka, 2008, Eq. (15)), plagioclase–melt (Waters and Lange, 2015), and clinopyroxene–melt (Putirka, 2008, Eq. (33)) thermometers. Host mineral–melt inclusion pairs are utilized to obtain estimates representative of the time of melt inclusion entrapment. Mean olivine–melt and plagioclase–melt temperatures are 1110–1140 °C and 1080–1130 °C, respectively. Sparse clinopyroxene–melt temperatures are lower at 1080 and 1120 °C. Late-stage temperature estimates obtained from mineral rim–matrix glass pairs are very similar, at 1110–1150 °C for the olivine–melt thermometer and 1100–1120 °C for the clinopyroxene–melt thermometer. Overall, our temperature estimates average at 1115 ± 30 °C and are consistent with previous results at Masaya (Bamber et al., 2020; de Moor et al., 2013). Although there is a slight tendency for Plinian samples to yield lower temperatures than lava lake samples, mean values typically overlap within one standard deviation and within the thermometers' standard errors of estimate, which range between ±12–30 °C (Putirka, 2008; Waters and Lange, 2015).
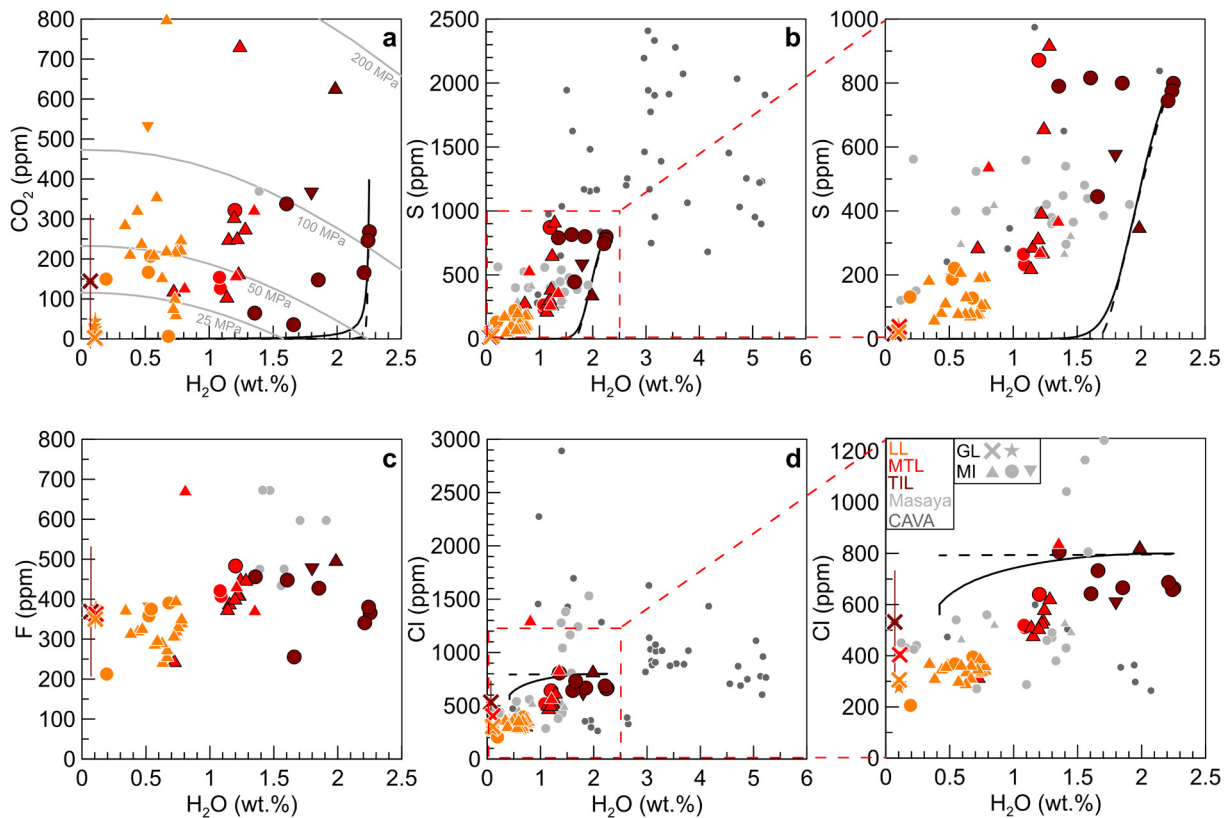
Fig. 6. Volatile element data for melt inclusions, matrix glasses, and Pele's hairs. Detailed symbology and published data sources as in Fig. 3, except published CO_2 data of Wehrmann et al. (2011). (a) CO_2 vs. H_2O concentrations, with 25, 50, 100 and 200 MPa isobars calculated with SolEx (Witham et al., 2011). (b) S vs. H_2O, with expanded inset, (c) F vs. H_2O, and (d) Cl vs. H_2O, with expanded inset. Plots also show degassing models calculated with SolEx (solid black line: closed system; dashed black line: open system; see text for details). Models use the average matrix glass composition and starting volatile contents of 400 ppm CO_2, 2.25 wt.% H_2O, 800 ppm S and 800 ppm Cl, which are representative of the most volatile-rich compositions observed (additional details in Supplements), at our mean temperature estimate of 1115 °C and an oxygen fugacity of FMQ + 1.7 (de Moor et al., 2013).
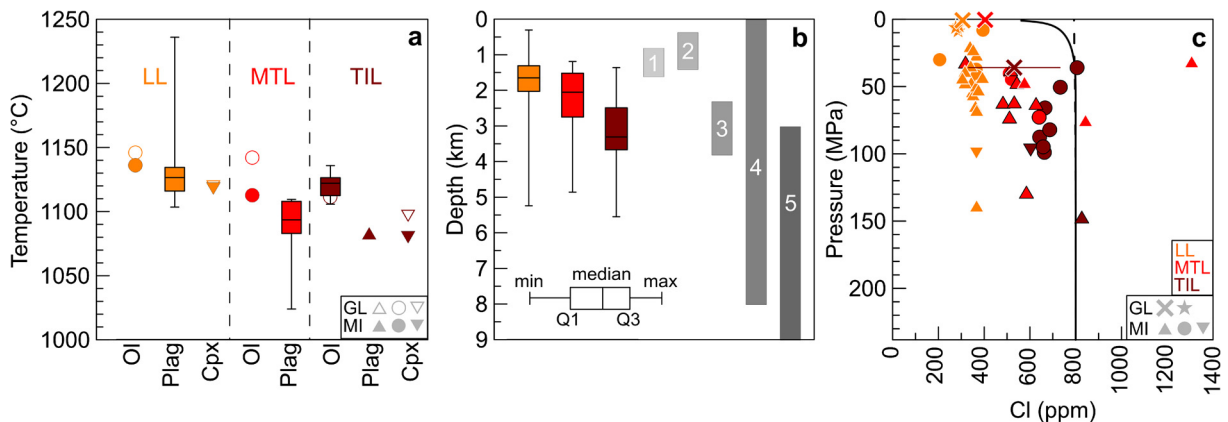

Fig. 7. Pre-eruptive temperature and pressure estimates. (a) Box and whisker plot of temperature estimates for lava lake and Plinian samples based on mineral–melt geothermometers (Putirka, 2008; Waters and Lange, 2015) using host mineral–melt inclusion pairs and mineral rim–matrix glass pairs. X-axis denotes mineral type. A symbol is shown when the minimum to maximum temperature range is smaller than symbol size (b) Box and whisker plot of melt inclusion entrapment/re-equilibration depths calculated from volatile saturation pressures, obtained from the model of Iacono-Marziano et al. (2012) and assuming a crustal density of 2,700 kg/m^3. Grayscale bars show published estimates of magma reservoir depths from (1) Bamber et al. (2020), (2) Aiuppa et al. (2018), and (3) Stephens and Wauthier (2018). Estimates from (4) Obermann et al. (2019) and (5) Métaxian (1994) include the shallow reservoir and a deeper sill body. (c) Volatile saturation pressure vs. Cl concentration for melt inclusions and matrix glasses. Closed- (solid black line) and open- (dashed black line) system degassing curves calculated with SolEx are shown for comparison (see Fig. 6 for details).

To estimate pressure, we use our measured CO_2 and H_2O contents in melt inclusions as input into the volatile solubility model of Iacono-Marziano et al. (2012). This generally yields low vapor saturation pressures (P_{sat}) in the range of 8–147 MPa (∼0.3–5.5 km), with only three melt inclusions giving values >100 MPa (Fig. 7b,c). Comparing eruptions, similar P_{sat} ranges are observed; however, only LL melt inclusions record values <31 MPa in the

uppermost kilometer of the plumbing system, and mean P_{sat} increase from 49 ± 28 MPa for LL, to 58 ± 25 MPa for MTL, and 84 ± 32 MPa for TIL. To a first order, we interpret these P_{sat} values to represent the magma storage pressures at which the melt inclusions were originally trapped or last re-equilibrated with the external melt (Fig. 6a). Such shallow magma storage pressures agree with prior petrologic (Bamber et al., 2020; Walker et
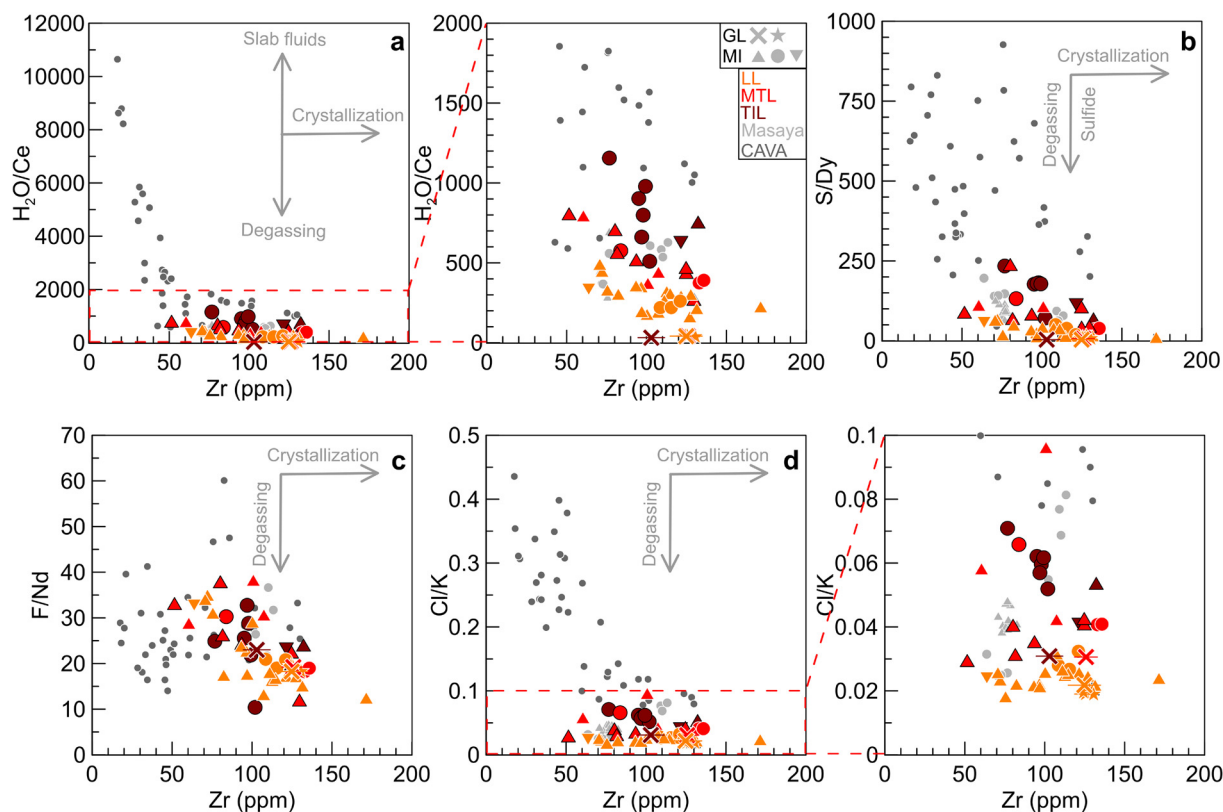
Fig. 8. Volatile–lithophile trace element ratios as a function of Zr concentration. Detailed symbology and published data sources as in Fig. 3. (a) H_2O/Ce, with expanded inset, (b) S/Dy, (c) F/Nd, and (d) Cl/K, with expanded inset, vs. Zr.

al., 1993) and geophysical (e.g., Obermann et al., 2019) studies (Fig. 7b).

4.2.2. Post-entrapment CO_2 and H_2O loss?

Before going further, however, two caveats to this interpretation should be discussed. First, several recent studies have shown that a large fraction of the originally dissolved CO_2 upon melt inclusion entrapment may later exsolve into vapor bubbles (e.g., Moore et al., 2015; Rasmussen et al., 2020; Venugopal et al., 2020). Some of our melt inclusions contain bubbles, and any post-entrapment CO_2 sequestration therein would lead to a significant P_{sat} underestimation. While this cannot be quantitatively evaluated without further analysis (e.g., Rasmussen et al., 2020), we note that all LL melt inclusions are bubble-free and thus record the total amount of CO_2 and that CO_2 concentrations in MTL bubble-free and bubble-bearing inclusions are in general agreement, suggesting negligible CO_2 loss to bubbles (see also section 4.2.3).

Second, it is also well-known that H_2O concentrations in melt inclusions can rapidly re-equilibrate with that of the external melt via post-entrapment H^+ diffusion through the host mineral (e.g., Gaetani et al., 2012; Lloyd et al., 2013). In our dataset, however, the preservation of correlations between H_2O and other volatiles and between H_2O and host anorthite content, which should be destroyed by extensive post-entrapment diffusive water loss, rules out this process as a dominant control on sample-to-sample variability (Figs. 6, S7d). This is further supported by the lack of correlation between melt inclusion size and H_2O content (Fig. S7b), because diffusive re-equilibration preferentially affects smaller inclusions (e.g., <30 μm), and is expected to yield positive trends between these variables (e.g., Lloyd et al., 2013; Barth et al., 2019). In detail, however, some within-sample variability may be due to water loss – particularly, the relatively wide range of H_2O/Ce values at near constant Zr concentration (∼100 ppm) displayed by a few of the TIL inclusions (Fig. 8).

4.2.3. Low-pressure degassing and halogens

Returning to our first-order interpretation, we conclude that the relatively low CO_2 and H_2O contents observed reflect extensive amounts of pre-eruptive degassing at low pressure, such that all Masaya melt inclusions record variably degassed melts mobilized from different depths within the shallow magmatic system. This is strongly indicated by the positive correlations between S, Cl and H_2O in our dataset (Fig. 6), which are best explained as degassing trends from a volatile-rich parental magma. Ratios of volatile and lithophile elements of similar bulk partition coefficients (H_2O/Ce, S/Dy, Cl/K and F/Nd) plotted against Zr concentrations further support this view (Fig. 8). Indeed, except for F/Nd, these ratios are typically much lower in Masaya melt inclusions than in other mafic Central American samples (Sadofsky et al., 2008), indicating that even our highest measured H_2O, S and Cl contents represent degassed values. Moreover, the negative correlations of H_2O/Ce, S/Dy, Cl/K and F/Nd versus Zr in the Masaya data demonstrate that melt inclusion entrapment occurred concomitantly to both crystallization and degassing of H_2O, S, Cl and F.

The evidence for substantial pre-eruptive degassing of halogens, consistent with Br and Cl data reported by Kutterolf et al. (2015), is particularly notable. Indeed, due to their comparatively high solubility in basaltic liquids, Cl and F typically remain largely dissolved in the melt during decompression-induced degassing until shallow crustal depths are reached (Webster et al., 2018, and references therein). For instance, melt inclusion data at Mount Etna indicate that Cl and F exsolution begins at pressures ≤100 MPa and ≤10 MPa, respectively, only becoming important during shallow degassing (Spilliaert et al., 2006). In addition, the experiments of Lesne et al. (2011), which were designed to simulate decompression-driven degassing on Masaya compositions, show that Cl degassing is insignificant at pressures ≥100 MPa, with modest Cl degassing only apparent for low-pressure experimental runs at 25 and 50 MPa. This is consistent with the general decrease

in Cl concentration with decreasing P_{sat} below 100 MPa observed in our dataset (Fig. 7c). In Fig. 6, we attempt to model observed degassing paths with SolEx (Witham et al., 2011), which incorporates Cl based on the data of Lesne et al. (2011). While neither open- nor closed-system degassing scenarios produce particularly good fits to the data, they do further support the contention that the significant pre-eruptive Cl degassing is a low-pressure (<100 MPa) feature (Fig. 7c).

Briefly, we note that our data also allow quantification of syn-eruptive degassing obtained by the widely-used "petrologic method" (e.g., Métrich and Wallace, 2008, and references therein). The calculations presented in full in the Supplements show that Plinian events release the equivalent of ∼5–11 years of quiescent degassing at Masaya based on modern averages (Aiuppa et al., 2019; cf. Burton et al., 2000; Zurek et al., 2019).

To sum up, the anomalously low concentrations of all (but F) volatiles in our melt inclusions compared to data from other mafic Central American volcanoes and the pre-eruptive degassing of the soluble halogens indicate that all Masaya magmas, irrespective of eruption style, endure copious amounts of degassing at shallow crustal depths before final ascent and eruption. Under such conditions, low, largely degassed CO_2 contents are expected, further suggesting that our P_{sat} values do not significantly suffer from potential CO_2 loss to bubbles. Our results are again in line with the findings of Walker et al. (1993) who showed that Masaya basalts fall near low-pressure cotectics, corroborating a central role for shallow processes in this system.

4.3. Estimates of undegassed H_2O contents

If all Masaya melt inclusions record extensive pre-eruptive degassing, a key question then follows: what are the primitive undegassed H_2O contents of Masaya magmas? In this section, we attempt to address this question from three different approaches, involving (1) calcium partitioning in olivine, (2) volcanic gas outputs, and (3) regional and global systematics of H_2O/Ce and Ba/La ratios in arc magmas.

First, as discussed by Gavrilenko et al. (2016), melt H_2O content influences olivine–melt calcium partitioning ($D_{CaO}^{Ol/L}$), and these authors' Ca-in-olivine geohygrometer may thus be used to obtain an independent estimate of H_2O content at Masaya at the time of olivine crystallization. Using Equations (1), (2) and (4) of Gavrilenko et al. (2016) and observed $CaO_{olivine}$, CaO_{melt} and MgO_{melt} of 0.17–0.31 wt.%, 8.7–11.8 wt.% and 4.5–9.8 wt.%, respectively, we calculate a "wet" $D_{CaO}^{Ol/L}$ of 0.02–0.03, a "dry" $D_{CaO}^{Ol/L}$ of 0.03–0.05, and a corresponding average melt H_2O content of 4.2 ± 1.3 wt.%.

Second, the volcano's prodigious gas emissions (e.g., Martin et al., 2010) may be used to back-calculate magmatic volatile concentrations. For H_2O, Burton et al. (2000) and Martin et al. (2010) respectively report fluxes of ∼12,000 t d^{-1} and ∼34,600 t d^{-1}. Assuming a magmatic source, 100% syn-eruptive degassing and a magma flux of 0.19 km^3 yr^{-1} obtained from sulfur outgassing (Zurek et al., 2019), these large H_2O fluxes require melt H_2O contents in the range of 2.3–6.6 wt.%.

Last but not least, an analysis of H_2O/Ce and Ba/La systematics at Masaya within the regional and global context is especially revealing (Fig. 9). Mafic Central American magmas typically have high H_2O/Ce ranging from ∼780 at Irazu to ∼12,850 at Cerro Negro, but mostly between 1500 and 4000 (Ruscitto et al., 2012; Sadofsky et al., 2008). Both in Central America and at the global scale, H_2O/Ce is broadly positively correlated with the Ba/La ratio, a traditional tracer of slab fluid contributions in arc magmas (Ruscitto et al., 2012). Yet, at Masaya, melt inclusions record some of the lowest H_2O/Ce (511 ± 354) and some of the highest Ba/La ratios (74 ± 11) of the global array. This paradox not only provides

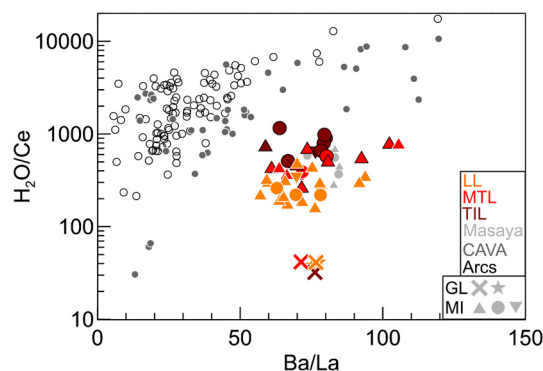**Fig. 9.** H_2O/Ce vs. Ba/La systematics. Detailed symbology and published data sources as in Fig. 3, except open black circles showing the global arc data of Ruscitto et al. (2012). Masaya samples show anomalously low H_2O/Ce for their Ba/La ratios. Note y-axis log scale.

additional evidence for pre-eruptive degassing lowering H_2O/Ce, but can also be exploited to reconstruct undegassed H_2O/Ce (and thus H_2O). For instance, the Ba/La–H_2O/Ce relationships of Ruscitto et al. (2012) (their Fig. 7a), with our mean Ba/La ratio of 74 ± 11 as input, predicts primitive H_2O/Ce values in the range of 6,820–16,480 at Masaya. With the mean Ce concentration of 23 ± 5 ppm in our samples, this would translate in H_2O contents in excess of 12 wt.%! Such values are likely unrealistically high (although see Steele-MacInnis, 2019, and references therein), perhaps due to regional variability in the subducting sediment composition raising Ba/La (Ruscitto et al., 2012), but they illustrate the point. In comparison, an expression (Ruscitto et al., 2012, their Fig. 8) based on the thermal slab parameter ($\Phi = 1100$ km for Nicaragua) yields H_2O/Ce of 2180–2430, corresponding to 3.9–6.8 wt.% H_2O for our samples.

Though variable, these three independent estimates overlap in a narrow range (3.9–5.5 wt.%) and all indicate undegassed water contents significantly exceeding our highest observed value. Pérez et al. (2020) reach a similar conclusion for Masaya's San Antonio Tephra for which they estimate an undegassed H_2O content of 5–6 wt.%.

4.4. Magma viscosity and microlite content

Recent studies have proposed that basaltic Plinian eruptions are related to a late-stage step increase in magma viscosity inducing fragmentation, brought about by abundant and rapid microlite crystallization during fast ascent of relatively cool (<1100 °C) and moderately hydrous (∼2 wt.% H_2O) basalt (Arzilli et al., 2019; Bamber et al., 2020). In this section, we briefly evaluate our samples in the light of these findings.

As shown in Fig. 7a, mean magma temperature estimates at Masaya approach the critical temperature proposed by Arzilli et al. (2019). However, temperature differences between lava lake and Plinian samples are subtle at most and thus cannot be called upon as primary eruptive style control. In terms of microlite content, preliminary analysis of backscattered electron (BSE) images of matrix glass chips yields 5 vol.% for LL, 15 vol.% for MTL, and 48 vol.% for TIL (Fig. S2). These values likely represent minima, however, since we preferentially selected glassier sample chips for chemical analysis. In comparison, for MTL glass, Bamber et al. (2020) identify heterogeneous textures, with 20–50 vol.% microlites, characterized by inter-mingled microlite-poor and microlite-rich zones bounded by submicron oxides.

Using the mean glass composition, water content and temperature for each eruption, we calculate melt viscosities of 10^2 Pa·s (for both LL and MTL) to 10^3 Pa·s (for TIL) with the model of Giordano et al. (2008). Integrating our estimated microlite contents to

the ConFlow 1.0.5 model (Mastin, 2002), minimum effective viscosities remain on the order of 10^2 Pa·s for both LL and MTL, but raise to 10^4 Pa·s for TIL, which is still 1–2 orders of magnitude short of the fragmentation threshold (Arzilli et al., 2019).

Nevertheless, the apparently contrasting textures of lava lake and Plinian samples, respectively microlite-poor and microlite-rich, are consistent with significant late-stage rheological changes in the conduit prior to explosive eruptions at Masaya (Arzilli et al., 2019; Bamber et al., 2020) and warrant further textural work. As suggested below, differing magma degassing histories and decompression paths imposed by the state of uppermost plumbing system may link sample textures and eruptive styles.

4.5. A thin line between open-conduit conditions and Plinian eruptions at Masaya?

Masaya is a highly unusual volcano associated with some of the most dramatic expressions of explosive basaltic volcanism on Earth (Pérez and Freundt, 2006; Pérez et al., 2020). The particularly sustained and voluminous supply of volatile-rich magma from depth (Martin et al., 2010; Zurek et al., 2019), which is likely ultimately controlled by complex local tectonics (Funk et al., 2009; Girard and van Wyk de Vries, 2005), must be in some way related to such sporadic, but long-lived explosive behavior. Yet, our data indicate that whether this vigorous magma supply translates to steady-state open-conduit conditions or explosive eruptions does not appear to be related to changes in the magmatic system at depth.

Indeed, our results reveal very little difference between magmas feeding the current lava lake and Holocene Plinian eruptions at Masaya. For both of these contrasting styles of activity, we infer that volatile-rich magma (3.9–5.5 wt.% H_2O) supplied from depth undergoes extensive pre-eruptive degassing and homogenization in a shallow (<4 km depth) magma reservoir before ascent to the surface. This is consistent with published petrologic, gas, geophysical, and structural data indicating the presence of a large, shallow reservoir beneath the caldera (Fig. 7b; e.g., Obermann et al., 2019; Zurek et al., 2019). Our data confirm that pre-eruptive dissolved volatile contents are not the culprit for eruptive style; basaltic arc magmas commonly show much higher volatile concentrations yet do not erupt as explosively as Masaya's (e.g., Roggensack et al., 1997). However, a key difference between lava lake and Plinian samples is their late-stage degassing history. Hence, we propose a model in which eruptive style is controlled in a top–down manner, whereby the state of the uppermost plumbing system modulates the late-stage decompression path of magma, and temporary sealing of the conduit may lead to transition to explosive behavior (Fig. 10).

During open-conduit conditions, volatile-rich magma from depth feeds into a shallow reservoir where a stable foam layer develops along its roof. Concurrently, within the open conduit, bi-directional convective flow allows the buoyant gas-rich magma to slowly ascend and degas quiescently to very low pressures, while gas-poor magma descends back into the reservoir, resulting in persistent degassing without eruption (Fig. 10a; Stix, 2007). This is reflected in LL melt inclusions which record extremely low volatile concentrations (<0.8 wt.% H_2O), corresponding to a P_{sat} range of 8–139 MPa (0.3–5.2 km). In turn, this slow magma ascent yields low degrees of undercooling and prevents significant microlite growth.

In contrast, the higher and distinct water contents and corresponding P_{sat} for MTL and TIL suggest that Plinian eruptions tap magma from varying, but slightly deeper depths within the shallow system compared to lava lake samples (Fig. 7b). The lack of P_{sat} estimates shallower than 31 MPa (1.2 km) indicates that the uppermost part of the plumbing system, i.e., the conduit, becomes efficiently sealed before Plinian events, such that magma is constrained to the main reservoir at 1–4 km depth (Fig. 10b). The cause of conduit sealing is unknown, but potential mechanisms include solidification due to a decrease in magma supply and/or plugging due to collapse (e.g., Roman et al., 2019). Under such a lid, degassing-induced pressure build-up and foam accumulation at the top of the shallow reservoir could prime the volcano for explosive eruption. Once overpressure exceeds the tensile stress of the overlying roof rocks and seal, catastrophic foam destabilization and explosive eruption occurs (Preece et al., 2016; Roman et al., 2019; Zhang, 1999). Magma coupled with the buoyant foam layer then rapidly ascends from the reservoir, at rates far exceeding those of open-conduit conditions, without time for additional melt inclusion entrapment or re-equilibration to occur in the shallow conduit (Fig. 10c). This rapid magma and foam ascent can yield high degrees of undercooling, triggering rapid microlite growth, which may in turn dramatically increase effective magma viscosity and eruption explosivity (Arzilli et al., 2019; Bamber et al., 2020; Shea and Hammer, 2013).

There may thus be a thin line between open-conduit conditions characterized by quiescent degassing and lava lake activity and transitions to highly explosive behavior at Masaya.

5. Conclusions

To evaluate the controls on eruptive style at Masaya volcano, we have constrained melt inclusion compositions, including dissolved CO_2, H_2O, S, Cl and F concentrations, and compared pre-eruptive magmatic conditions for the recent lava lake and two Holocene Plinian eruptions—the Masaya Triple Layer and Ticuantepe Lapilli. Though systematically higher than those of lava lake samples, pre-eruptive volatile contents for Plinian tephras are low compared to typical arc magmas and cannot be invoked as the culprit for Masaya's unusually explosive behavior. Melt inclusions reveal low-pressure degassing trends confirming that all Masaya magmas, regardless of eruptive style, experience extensive degassing in a shallow reservoir (1–4 km depth) before being mobilized to the surface. In contrast to lava lake samples, however, melt inclusions from Plinian samples do not record the lowest pressures corresponding to the open conduit (<1 km), suggesting it had become sealed to shallow magma convective flow. We therefore postulate that transitions between open-conduit and Plinian activity at Masaya only require subtle changes in the geometry of the volcano's uppermost magma plumbing system. Temporary plugging of the conduit coupled with vigorous gas accumulation would result in efficient overpressurization in the magma reservoir. Sudden rupture of the seal could then cascade into catastrophic foam destabilization and rapid magma ascent, which would preclude timely gas–melt separation and yield large degrees of undercooling, favoring late-stage microlite growth and thus enabling magma fragmentation and explosive eruption.

CRediT authorship contribution statement

M.-A.L. conceptualized the project and methodological design. W.P. and S.K. provided Plinian tephra samples. L.H. prepared samples and performed SIMS, EPMA, and LA-ICP-MS data collection and analysis. B.M. oversaw SIMS data collection. L.H. prepared figures and wrote the original manuscript, with contributions from M.-A.L. All authors reviewed and provided input on the final manuscript.

Declaration of competing interest

The authors declare that they have no known competing financial interests or personal relationships that could have appeared to influence the work reported in this paper.
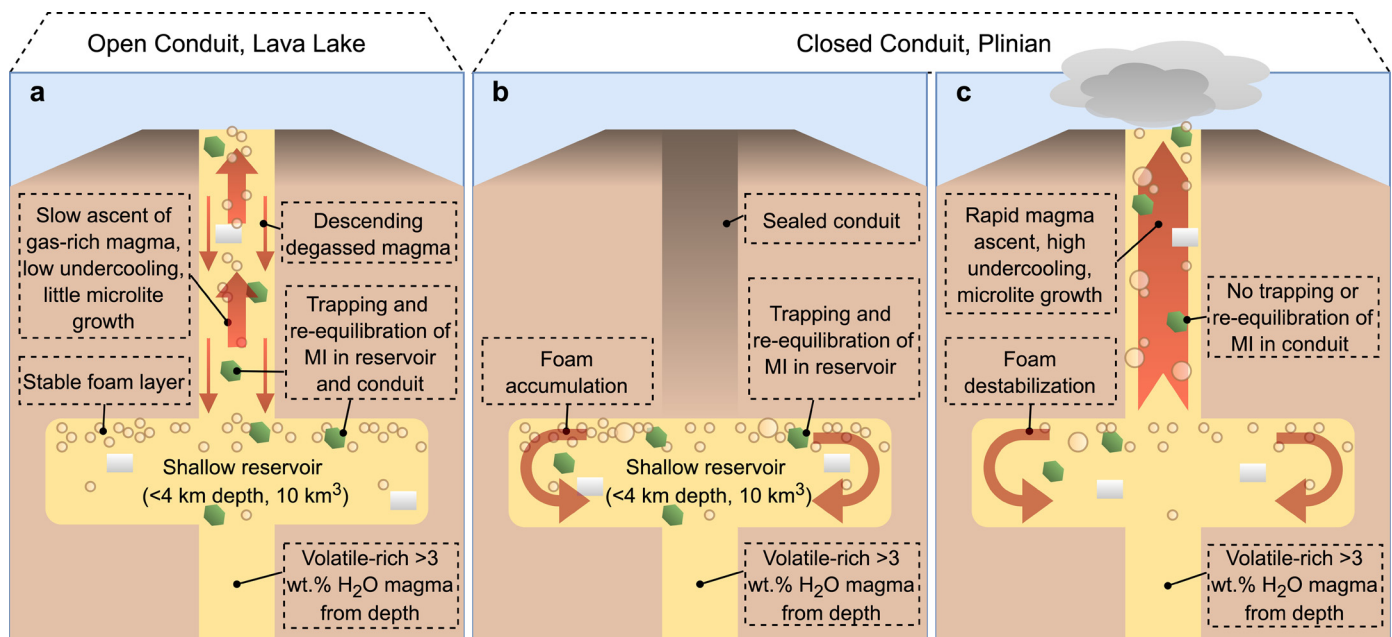
Fig. 10. Schematic diagram illustrating the proposed top–down control on eruptive style at Masaya volcano (modified from Stix, 2007). (a) During open-conduit conditions, deep-sourced volatile-rich magma ascends to a large, shallow (<4 km) reservoir connected to the surface via a conduit in which bi-directional convective flow occurs. Melt inclusion trapping and/or re-equilibration take place at various levels within the reservoir and conduit. Magma ascent in the conduit is comparatively slow, keeping undercooling low and preventing extensive microlite crystallization. (b) Plugging in uppermost plumbing system seals the conduit, and magma is restrained to the reservoir, where melt inclusions form. Under such closed-conduit conditions, high gas accumulation rates in the shallow reservoir lead to pressure build-up. (c) The seal breaks, triggering catastrophic foam destabilization and rapid magma ascent — too fast to allow additional melt inclusion trapping or re-equilibration. This rapid magma decompression yields high degrees of undercooling and promotes microlite growth. Pink circles, green hexagons and white rectangles respectively represent bubbles and melt inclusion host minerals.

Acknowledgements

Appendix A. Supplementary material

Supplementary material related to this article can be found online at https://doi.org/10.1016/j.epsl.2021.117138.

References

Aiuppa, A., de Moor, J.M., Arellano, S., Coppola, D., Francofonte, V., Galle, B., Giudice, G., Liuzzo, M., Mendoza, E., Saballos, A., Tamburello, G., Battaglia, A., Bitetto, M., Gurrieri, S., Laiolo, M., Mastrolia, A., Moretti, R., 2018. Tracking formation of a Lava Lake from ground and space: Masaya Volcano (Nicaragua), 2014–2017. Geochem. Geophys. Geosyst., 496–515. https://doi.org/10.1002/2017GC007227.

Aiuppa, A., Fischer, T.P., Plank, T., Bani, P., 2019. CO_2 flux emissions from the Earth's most actively degassing volcanoes, 2005–2015. Sci. Rep. 9, 5442. https://doi.org/10.1038/s41598-019-41901-y.

Arzilli, F., La Spina, G., Burton, M.R., Polacci, M., Le Gall, N., Hartley, M.E., Di Genova, D., Cai, B., Vo, N.T., Bamber, E.C., Nonni, S., Atwood, R., Llewellin, E.W., Brooker, R.A., Mader, H.M., Lee, P.D., 2019. Magma fragmentation in highly explosive basaltic eruptions induced by rapid crystallization. Nat. Geosci. 12, 1023–1028. https://doi.org/10.1038/s41561-019-0468-6.

Bamber, E.C., Arzilli, F., Polacci, M., Hartley, M.E., Fellowes, J., Di Genova, D., Chavarría, D., Saballos, J.A., Burton, M.R., 2020. Pre- and syn-eruptive conditions of a basaltic Plinian eruption at Masaya Volcano, Nicaragua: the Masaya Triple Layer (2.1 ka). J. Volcanol. Geotherm. Res. 392, 106761. https://doi.org/10.1016/j.jvolgeores.2019.106761.

Barth, A., Newcombe, M., Plank, T., Gonnermann, H., Hajimirza, S., Soto, G.J., Saballos, A., Hauri, E., 2019. Magma decompression rate correlates with explosivity at basaltic volcanoes — constraints from water diffusion in olivine. J. Volcanol. Geotherm. Res. 387, 106664. https://doi.org/10.1016/j.jvolgeores.2019.106664.

Burton, M.R., Horrocks, L.A., Francis, P.W., 2000. Remote sensing of CO2 and H2O emission rates from Masaya volcano Nicaragua. Geology 28, 915–918. https://doi.org/10.1130/0091-7613(2000)28<915:RSOCAH>2.0.CO;2.

Carr, M.J., 1984. Symmetrical and segmented variation of physical and geochemical characteristics of the central American Volcanic front. J. Volcanol. Geotherm. Res. 20, 231–252. https://doi.org/10.1016/0377-0273(84)90041-6.

Carr, M.J., Feigenson, M.D., Bolge, L.L., Walker, J.A., Gazel, E., 2014. RU_CAGeochem, a database and sample repository for central American volcanic rocks at Rutgers University. Geosci. Data J. 1, 43–48. https://doi.org/10.1002/gdj3.10.

Cassidy, M., Manga, M., Cashman, K., Bachmann, O., 2018. Controls on explosive-effusive volcanic eruption styles. Nat. Commun. 9, 2839. https://doi.org/10.1038/s41467-018-05293-3.

Costantini, L., Houghton, B.F., Bonadonna, C., 2010. Constraints on eruption dynamics of basaltic explosive activity derived from chemical and microtextural study: the example of the Fontana Lapilli Plinian Eruption, Nicaragua. J. Volcanol. Geotherm. Res. 189, 207–224. https://doi.org/10.1016/j.jvolgeores.2009.11.008.

Danyushevsky, L.V., Plechov, P., 2011. Petrolog3: integrated software for modeling crystallization processes. Geochem. Geophys. Geosyst. 12, 1–32. https://doi.org/10.1029/2011GC003516.

de Moor, J.M., Fischer, T.P., Sharp, Z.D., King, P.L., Wilke, M., Botcharnikov, R.E., Cottrell, E., Zelenski, M., Marty, B., Klimm, K., Rivard, C., Ayalew, D., Ramirez, C., Kelley, K.A., 2013. Sulfur degassing at Erta Ale (Ethiopia) and Masaya (Nicaragua) volcanoes: implications for degassing processes and oxygen fugacities of basaltic systems. Geochem. Geophys. Geosyst. 14, 4076–4108. https://doi.org/10.1002/ggge.20255.

Francis, P., Oppenheimer, C., Stevenson, D., 1993. Endogenous growth of persistently active volcanoes. Nature 366, 554–557. https://doi.org/10.1038/366554a0.

Funk, J., Mann, P., McIntosh, K., Stephens, J., 2009. Cenozoic tectonics of the Nicaraguan depression, Nicaragua, and Median trough, El Salvador, based on seismic-reflection profiling and remote-sensing data. Bull. Geol. Soc. Am. 121, 1491–1521. https://doi.org/10.1130/B26428.1.

Gaetani, G.A., O'Leary, J.A., Shimizu, N., Bucholz, C.E., Newville, M., 2012. Rapid reequilibration of H_2O and oxygen fugacity in olivine-hosted melt inclu-

sions. Geology 40 (10), 915–918. ISSN 0091-7613. https://resolver.caltech.edu/CaltechAUTHORS:20180111-162501944.

Gavrilenko, M., Herzberg, C., Vidito, C., Carr, M.J., Tenner, T., Ozerov, A., 2016. A calcium-in-olivine geohygrometer and its application to subduction zone magmatism. J. Petrol. 57, 1811–1832. https://doi.org/10.1093/petrology/egw062.

Giordano, D., Russell, J.K., Dingwell, D.B., 2008. Viscosity of magmatic liquids: a model. Earth Planet. Sci. Lett. 271, 123–134. https://doi.org/10.1016/j.epsl.2008.03.038.

Girard, G., van Wyk de Vries, B., 2005. The Managua Graben and Las Sierras-Masaya volcanic complex (Nicaragua); pull-apart localization by an intrusive complex: results from analogue modeling. J. Volcanol. Geotherm. Res. 144, 37–57. https://doi.org/10.1016/j.jvolgeores.2004.11.016.

Goepfert, K., Gardner, J.E., 2010. Influence of pre-eruptive storage conditions and volatile contents on explosive Plinian style eruptions of basic magma. Bull. Volcanol. 72, 511–521. https://doi.org/10.1007/s00445-010-0343-1.

Gregg, T.K.P., Williams, S.N., 1996. Explosive mafic volcanoes on Mars and Earth: deep magma sources and rapid rise rate. Icarus 122, 397–405. https://doi.org/10.1006/icar.1996.0132.

Hauri, E., Wang, J., Dixon, J.E., King, P.L., Mandeville, C., Newman, S., 2002. SIMS analysis of volatiles in silicate glasses 1. Calibration, matrix effects and comparisons with FTIR. Chem. Geol. 183, 99–114. https://doi.org/10.1016/S0009-2541(01)00375-8.

Helo, C., Longpré, M., Shimizu, N., Clague, D.A., Stix, J., 2011. Explosive eruptions at mid-ocean ridges driven by CO_2-rich magmas. Nat. Geosci. 4, 260–263. https://doi.org/10.1038/ngeo1104.

Houghton, B.F., Gonnermann, H.M., 2008. Basaltic explosive volcanism: constraints from deposits and models. Geochemistry 68, 117–140. https://doi.org/10.1016/j.chemer.2008.04.002.

Iacono-Marziano, G., Morizet, Y., Le Trong, E., Gaillard, F., 2012. New experimental data and semi-empirical parameterization of H_2O-CO_2 solubility in mafic melts. Geochim. Cosmochim. Acta 97, 1–23. https://doi.org/10.1016/j.gca.2012.08.035.

Kutterolf, S., Freundt, A., Schacht, U., Burk, D., Harders, R., Morz, T., Pérrez, W., 2008. Pacific offshore record of plinian arc volcanism in central America: 3. Application to forearc geology. Geochem. Geophys. Geosyst. 9, 1–14. https://doi.org/10.1029/2007GC001826.

Kutterolf, S., Hansteen, T.H., Freundt, A., Wehrmann, H., Appel, K., Krüger, K., Pérez, W., 2015. Bromine and chlorine emissions from Plinian eruptions along the central American Volcanic Arc: from source to atmosphere. Earth Planet. Sci. Lett. 429, 234–246. https://doi.org/10.1016/j.epsl.2015.07.064.

Lesne, P., Kohn, S.C., Blundy, J., Witham, F., Botcharnikov, R.E., Behrens, H., 2011. Experimental simulation of closed-system degassing in the system basalt-H_2O-CO_2-S-Cl. J. Petrol. 52, 1737–1762. https://doi.org/10.1093/petrology/egr027.

Lloyd, A.S., Plank, T., Ruprecht, P., Hauri, E.H., Rose, W., 2013. Volatile loss from melt inclusions in pyroclasts of differing sizes. Contrib. Mineral. Petrol. 165, 129–153. https://doi.org/10.1007/s00410-012-0800-2.

Longpré, M.A., Stix, J., Klügel, A., Shimizu, N., 2017. Mantle to surface degassing of carbon- and sulphur-rich alkaline magma at El Hierro, Canary Islands. Earth Planet. Sci. Lett. 460, 268–280. https://doi.org/10.1016/j.epsl.2016.11.043.

Martin, R.S., Sawyer, G.M., Spampinato, L., Salerno, G.G., Ramirez, C., Ilyinskaya, E., Witt, M.L.I., Mather, T.A., Watson, I.M., Phillips, J.C., Oppenheimer, C., 2010. A total volatile inventory for Masaya Volcano, Nicaragua. J. Geophys. Res., Solid Earth 115, 1–12. https://doi.org/10.1029/2010JB007480.

Mastin, L.G., 2002. Insights into volcanic conduit flow from an open-source numerical model. Geochem. Geophys. Geosyst. 3, 1–18. https://doi.org/10.1029/2001GC000192.

McDonough, W.F., Sun, S.S., 1995. The composition of the Earth. Chem. Geol. 120, 223–253. https://doi.org/10.1016/0009-2541(94)00140-4.

Métaxian, J., 1994. Etude sismologique et gravimetrique d'un volcano actif: Dynamisme interne et structure de la Caldeira Masaya, Nicaragua. Ph.D. thesis. Université de Savoie, France. http://www.theses.fr/1994CHAMA001.

Métrich, N., Wallace, P.J., 2008. Volatile abundances in basaltic magmas and their degassing paths tracked by melt inclusions. Rev. Mineral. Geochem. 69, 363–402. https://doi.org/10.2138/rmg.2008.69.10.

Moitra, P., Gonnermann, H.M., Houghton, B.F., Tiwary, C.S., 2018. Fragmentation and Plinian eruption of crystallizing basaltic magma. Earth Planet. Sci. Lett. 500, 97–104. https://doi.org/10.1016/j.epsl.2018.08.003.

Moore, L.R., Gazel, E., Tuohy, R., Lloyd, A., Esposito, R., Steele-McInnis, M., Hauri, E., Wallace, P., Plank, T., Bodnar, R., 2015. Bubbles matter: an assessment of the contribution of vapor bubbles to melt inclusion volatile budgets. Am. Mineral. 100, 806–823. https://doi.org/10.2138/am-2015-5036.

Obermann, A., Molinari, I., Métaxian, J.P., Grigoli, F., Strauch, W., Wiemer, S., 2019. Structure of Masaya and Momotombo volcano, Nicaragua, investigated with a temporary seismic network. J. Volcanol. Geotherm. Res. 379, 1–11. https://doi.org/10.1016/j.jvolgeores.2019.04.013.

Pérez, Fernández Wendy, 2007. Basaltic Plinian and violent Surtseyan eruptions from the Masaya Caldera Complex, Nicaragua. PhD thesis. University of Kiel. 195 pp. https://nbn-resolving.org/urn:nbn:de:gbv:8-diss-20637.

Pérez, W., Freundt, A., 2006. The youngest highly explosive basaltic eruptions from Masaya Caldera (Nicaragua): stratigraphy and hazard assessment. In: Geological Society of America Special Papers, pp. 189–207.

Pérez, W., Freundt, A., Kutterolf, S., Schmincke, H.U., 2009. The Masaya Triple Layer: a 2100 year old basaltic multi-episodic Plinian eruption from the Masaya Caldera Complex (Nicaragua). J. Volcanol. Geotherm. Res. 179, 191–205. https://doi.org/10.1016/j.jvolgeores.2008.10.015.

Pérez, W., Freundt, A., Kutterolf, S., 2020. The basaltic plinian eruption of the ~6 ka San Antonio Tephra and formation of the Masaya caldera, Nicaragua. J. Volcanol. Geotherm. Res. 401, 106975. https://doi.org/10.1016/j.jvolgeores.2020.106975.

Preece, K., Gertisser, R., Barclay, J., Charbonnier, S.J., Komorowski, J.C., Herd, R.A., 2016. Transitions between explosive and effusive phases during the cataclysmic 2010 eruption of Merapi volcano, Java, Indonesia. Bull. Volcanol. 78, 54. https://doi.org/10.1007/s00445-016-1046-z.

Putirka, K.D., 2008. Thermometers and Barometers for volcanic systems. Rev. Mineral. Geochem. 69, 61–120. https://doi.org/10.2138/rmg.2008.69.3.

Rasmussen, D.J., Plank, T.A., Wallace, P.J., Newcombe, M.E., Lowenstern, J.B., 2020. Vapor-bubble growth in olivine-hosted melt inclusions. Am. Mineral. 105, 1898–1919. https://doi.org/10.2138/am-2020-7377.

Roggensack, K., Hervig, R.L., McKnight, S.B., Williams, S.N., 1997. Explosive basaltic volcanism from Cerro Negro volcano: influence of volatiles on eruptive style. Science 277, 1639–1642. https://doi.org/10.1126/science.277.5332.1639.

Roman, D.C., LaFemina, P.C., Bussard, R., Stephens, K., Wauthier, C., Higgins, M., Feineman, M., Arellano, S., de Moor, J.M., Avard, G., Cruz, M.M., Burton, M., Varnam, M., Saballos, A., Ibarra, M., Strauch, W., Tenorio, V., 2019. Mechanisms of Unrest and Eruption at Persistently Restless Volcanoes: insights from the 2015 Eruption of Telica Volcano, Nicaragua. Geochem. Geophys. Geosyst. 20, 4162–4183. https://doi.org/10.1029/2019GC008450.

Ruscitto, D.M., Wallace, P.J., Cooper, L.B., Plank, T., 2012. Global variations in H_2O/Ce: 2. Relationships to arc magma geochemistry and volatile fluxes. Geochem. Geophys. Geosyst. 13. https://doi.org/10.1029/2011GC003887.

Sadofsky, S.J., Portnyagin, M., Hoernle, K., van den Bogaard, P., 2008. Subduction cycling of volatiles and trace elements through the central American volcanic arc: evidence from melt inclusions. Contrib. Mineral. Petrol. 155, 433–456. https://doi.org/10.1007/s00410-007-0251-3.

Shea, T., Hammer, J.E., 2013. Kinetics of cooling- and decompression-induced crystallization in hydrous mafic-intermediate magmas. J. Volcanol. Geotherm. Res. 260, 127–145. https://doi.org/10.1016/j.jvolgeores.2013.04.018.

Shinohara, H., 2008. Excess degassing from volcanoes and its role on eruptive and intrusive activity. Rev. Geophys. 46, 1–31. https://doi.org/10.1029/2007RG000244.

Sides, I.R., Edmonds, M., Maclennan, J., Swanson, D.A., Houghton, B.F., 2014. Eruption style at Kilauea Volcano in Hawai'i linked to primary melt composition. Nat. Geosci. 7, 464–469. https://doi.org/10.1038/ngeo2140.

Spilliaert, N., Métrich, N., Allard, P., 2006. S-Cl-F degassing pattern of water-rich alkali basalt: modelling and relationship with eruption styles on Mount Etna volcano. Earth Planet. Sci. Lett. 248, 772–786. https://doi.org/10.1016/j.epsl.2006.06.031.

Steele-MacInnis, M., 2019. Seeking the most hydrous, primitive arc melts: the glass is half full. Am. Mineral. 104, 1217–1218. https://doi.org/10.2138/am-2019-7124.

Stephens, K.J., Wauthier, C., 2018. Satellite geodesy captures offset magma supply associated with lava lake appearance at Masaya Volcano, Nicaragua. Geophys. Res. Lett. 45, 2669–2678. https://doi.org/10.1002/2017GL076769.

Stix, J., 2007. Stability and instability of quiescently active volcanoes: the case of Masaya, Nicaragua. Geology 35, 535–538. https://doi.org/10.1130/G23198A.1.

Venugopal, S., Schiavi, F., Moune, S., Bolfan-Casanova, N., Druitt, T., Williams-Jones, G., 2020. Melt inclusion vapour bubbles: the hidden reservoir for major and volatile elements. Sci. Rep. 10, 1–14. https://doi.org/10.1038/s41598-020-65226-3.

Walker, J.A., Williams, S.N., Kalamarides, R.I., Feigenson, M.D., 1993. Shallow open-system evolution of basaltic magma beneath a subduction zone volcano: the Masaya Caldera complex, Nicaragua. J. Volcanol. Geotherm. Res. 56, 379–400. https://doi.org/10.1016/0377-0273(93)90004-B.

Waters, L.E., Lange, R.A., 2015. An updated calibration of the plagioclase-liquid hygrometer-thermometer applicable to basalts through rhyolites. Am. Mineral. 100, 2172–2184. https://doi.org/10.2138/am-2015-5232.

Webster, J.D., Baker, D.R., Aiuppa, A., 2018. Halogens in mafic and intermediate-silica content magmas. In: Harlov, D.E., Aranovich, L. (Eds.), The Role of Halogens in Terrestrial and Extraterrestrial Geochemical Processes. In: Springer Geochemistry. Springer, Cham.

Wehrmann, H., Hoernle, K.A., Portnyagin, M.V., Wiedenbeck, M., Heydolph, K., 2011. Volcanic CO_2 output at the central American subduction zone inferred from melt inclusions in olivine crystals from mafic tephras. Geochem. Geophys. Geosyst. 12. https://doi.org/10.1029/2010GC003412.

Williams, S.N., 1983. Plinian airfall deposits of basaltic composition. Geology 11, 211–214. https://doi.org/10.1130/0091-7613(1983)11<211:PADOBC>2.0.CO;2.

Witham, F., Blundy, J., Kohn, S.C., Lesne, P., Dixon, J., Churakov, S.V., Botcharnikov, R., 2011. Computers & geosciences SolEx: a model for mixed COHSCl-volatile solu-

bilities and exsolved gas compositions in basalt. Comput. Geosci., 1–11. https://doi.org/10.1016/j.cageo.2011.09.021.

Zhang, Y., 1999. A criterion for the fragmentation of bubbly magma based on brittle failure theory. Nature 402, 648–650. https://doi.org/10.1038/45210.

Zurek, J., Moune, S., Williams-Jones, G., Vigouroux, N., Gauthier, P.J., 2019. Melt inclusion evidence for long term steady-state volcanism at Las Sierras-Masaya volcano, Nicaragua. J. Volcanol. Geotherm. Res. 378, 16–28. https://doi.org/10.1016/j.jvolgeores.2019.04.007.